

UNIVERSITY OF CALIFORNIA SAN DIEGO

COMPARISON OF IMAGE PROCESSING TECHNIQUES FOR SKIN CANCER
SEGMENTATION & CLASSIFICATION USING MATLAB

BY

VERONICA MARROCCO

AUGUST 2025

1. Abstract

Melanoma is the deadliest form of skin cancer, yet is highly curable if detected early [1, 3]. However, limited access to dermatologists and variability in lesion presentation motivate the development of accessible, automated diagnostic tools. This work presents a MATLAB-based application for skin lesion segmentation and classification, designed to operate on standard photographs without dermoscopy. The system integrates five complementary segmentation algorithms: Otsu thresholding, adaptive thresholding, active contour (Chan-Vese), seeded region growing, and K-means clustering in a chromatic-spatial feature space. Users can visually compare segmentation outputs and select the most accurate mask, after which the program extracts clinically relevant features. These features are scored using a modified ABCDE framework that replaces ‘Diameter’ with ‘Darkness’ and employs a weighted ABC-point list scheme to generate a total diagnostic score (TDS), categorizing lesions as likely malignant, suspicious, or likely benign.

Evaluation on a manually curated dataset of 71 images spanning diverse skin tones, lesion types and image conditions, yielded a sensitivity of 94.87% and specificity of 93.33%, with relatively low false positive (6.67%) and false negative (5.13%) rates. Otsu thresholding produced the highest proportion of optimal masks overall, while region growing empirically performed best on darker skin tones. Results demonstrate that combining multiple segmentation paradigms with user-guided mask selection improves robustness across variable imaging conditions and patient demographics. Future work will focus on expanding the dataset for results’ generalizability and automating optimal mask selection via machine learning models whose cost functions correlate with mask quality, ultimately enabling transition toward a fully automated melanoma screening tool.

2. Background

Skin cancer is the most commonly diagnosed type of cancer across all populations, regardless of age, gender, or race [1]. Among its various forms, melanoma is the most deadly, and its incidence has been rapidly increasing over the last few decades [2]. Paradoxically, melanoma is also a highly treatable cancer, if diagnosed at an early stage. According to U.S. epidemiological data, the 5-year survival rate for localized melanoma exceeds 99%, but plummets to just 25% once the cancer has metastasized [3]. This disparity underscores the life-saving potential of early and accurate diagnosis. However, access to dermatologists remains limited, especially in rural and underserved regions. With dermatology consultation costs averaging over \$200 per visit in the U.S. [4], and long wait times for specialist referrals, there is increasing interest in affordable, accessible, and automated diagnostic systems that can aid in the early detection of melanoma. The benefits of such systems are two fold: (1) to offer quantitative information about a lesion that can be relevant for the dermatologist; (2) to be used as a standalone early warning tool for individuals, in the absence of a dermatologist. Additionally, independent diagnostic systems have the potential to improve clinical outcomes by reducing dependency on human observation [9], and offering consistent, quantitative assessment of skin lesions [3].

2.1. Diagnostic Frameworks

Currently, the diagnosis of melanoma often relies on visual inspection of the lesion and pattern recognition by a trained dermatologist. Several score-based diagnostic frameworks have been developed to assist with lesion evaluation, among which is the ABCD rule, introduced by Stolz et al. and Nachbar et al. [5, 6]. The traditional ABCD system evaluates four key morphological features of pigmented lesions in a semi-quantitative fashion:

1. **Asymmetry (0-2):** Lesions are assessed for asymmetry along the major axes, with malignant lesions typically exhibiting more asymmetrical shapes.
2. **Border Irregularity (0-8):** The edges of malignant lesions tend to be poorly defined and fuzzy, in contrast to the smoother, more uniform borders seen in benign nevi.

3. **Color Variation (1-6):** Benign lesions typically contain one or two uniform colors, whereas melanomas often contain three or more colours such as tan, brown, black, red, white or blue gray.
4. **Diameter (in mm):** Traditionally, lesions with diameter > 6mm have been considered particularly suspicious.

Each of these features in the ABCD rule is assigned a numerical value based on severity and weighted to generate a final total diagnostic score (TDS) according to the following equation: $TDS = (A \times 1.3) + (B \times 0.1) + (C \times 0.5) + (D \times 0.5)$.

Recent literature has introduced several enhancements and simplifications to classical ABCD methods. One such algorithm is the ABC-Point List and modified ABC-Point List which aims to simplify the ABCD rule and improve diagnostic accuracy [7, 8]. In addition to these approaches, the ABCD criteria have been expanded to include an “E” for evolution, reflecting the importance of lesion changes over time [10]. “Evolving lesions” are defined as those encompassing recent changes in size, shape, symptoms (e.g., itching, tenderness), color shades and surface characteristics (e.g., scaling, bleeding). Clinically, evolution has independently been found to be the most important predictor of melanoma in patient-observed features [11]. To incorporate this clinically meaningful information into the TDS equation, the “E” feature is assigned a discrete score of -1, 0 or 1, where a score of 1 indicates clear progression or change, 0 indicates uncertain information, and -1 indicates stability [10].

Emerging evidence also suggests that diameter may not be the most reliable criterion for evaluation, as many early-stage melanomas are detected below this size, while some benign lesions may exceed it [13]. In fact, the existence of small (< 6mm) melanomas is well documented [13, 15], indicating that the ABCDE rule’s diameter requirement should be modified. Recent studies further emphasize that many melanomas, specifically small melanomas, can be recognized because of, and only because of, their intensity of pigment, i.e. darkness [14], rather than by size. Despite this, darkness has been traditionally underrepresented in the clinical criteria. Newer diagnostic frameworks have adapted the ABCDE rule to incorporate ‘Darkness’ explicitly in place of, or alongside, diameter. The Skin Cancer Foundation, for example, updated

their guidelines to acknowledge that the ‘D’ in ABCDE can stand for both Diameter and Darkness [15].

2.2. Automated Diagnostic Systems

Automated diagnostic systems can be implemented via user-facing software that uses simple image processing techniques to accurately diagnose melanoma in its early stages [16]. Currently, the standard approach used for automatic image analysis consists of three stages: (i) image segmentation, (ii) feature extraction and (iii) lesion classification [16]. The system will automatically extract key morphological features from the lesion, namely asymmetry, border irregularity, and color variation, and use them to score the lesion using a modified ABCDE scale, which no longer considers lesion diameter, but rather darkness. Based on these scores, the tool will classify the lesion as benign, suspicious, or malignant.

2.3. Image Segmentation

A key challenge in building robust, generalizable lesion analysis tools lies in the segmentation step, where the lesion must be accurately isolated from the surrounding skin. Due to large variability in skin tone, lighting conditions, image quality, and lesion appearance (e.g., dirt, blurred edges or hair occlusion), no single segmentation algorithm consistently performs well across all image types.

Thresholding algorithms, such as Otsu’s method [18, 19] or adaptive local thresholding [20, 21], are simple and computationally efficient. In global thresholding, like Otsu’s method, a single threshold value is computed and applied to the entire image, while adaptive (local) thresholding calculates thresholds for smaller blocks within the image, allowing the method to compensate for uneven illumination or gradual intensity changes. In either case, a binary image is produced by grouping pixels into two classes, based on whether it is below or above the specified local or global threshold value. These algorithms have been shown to achieve high accuracy when the lesion has consistent characteristics and the surrounding skin regions are homogeneous in nature, meaning the corresponding image histogram is bimodal [22]. However, difficulties arise in situations characterized by structural, illumination and color variations, when

the modes from the two regions overlap and thus no clear histogram threshold can be found that separates the lesion regions from the surrounding skin [20].

In relation to image processing, clustering is often referred to as a multidimensional extension of thresholding. Clustering based lesion segmentation techniques, such as K-means [23, 24], group pixels in multidimensional feature space (e.g., color plus spatial coordinates) without requiring explicitly defined thresholds, allowing complex boundaries to be captured. K-means is an unsupervised machine learning clustering approach in which the algorithm “learns” the optimal decision boundaries, or multidimensional thresholds, between pixel groups directly from the data, giving it the ability to handle lesions with heterogeneous color distributions and irregular shapes. However, because this type of clustering is driven primarily by chromatic similarity, with spatial information used only as one of the weighted features rather than a strict connectivity requirement, the resulting lesion mask may be spatially fragmented or contain small, disjoint regions, often necessitating significant post-processing to merge components [25].

Next, region-based techniques, such as seeded region growing [26, 27], expand from an initial seed pixel by grouping spatially connected pixels with similar properties, allowing edges to be detected even when contrast is low. However, these methods can be sensitive to noise and over segmentation in cases where illumination varies significantly across the lesion, or where there is substantial chromatic or textural heterogeneity [28].

Finally, active contour models (snakes) [29] evolve a deformable curve toward the boundaries of the skin lesion regions. While typically more robust than thresholding at handling noise, artifacts and variations in illumination, active contour approaches can face difficulties in situations characterized by weak contrast between the skin lesions and the surrounding skin regions, or when boundaries are ill-defined [29].

The latest review by Mendonça et al. [20] on computational methods for lesion segmentation found adaptive thresholding to produce the most favorable automatic segmentation results, while robust snake achieved a more consistent performance. In utter contrast, Silveira et al. [21] reported that adaptive thresholding as well as Chan-Vese active contour models [30] yielded the least satisfactory outcomes. These conflicting findings highlight the inconsistency of current segmentation methods in performing optimally across all images, underscoring the value

of a system that allows the user to visually assess and select the method that has performed best for a given image input.

2.4. Project Aim

The goal of this project is to develop a MATLAB-based diagnostic application that allows users to interactively segment a skin lesion image using multiple complementary methods, compare the resulting masks, and select the most accurate one for further analysis. This graphical user interface (GUI) will support multiple segmentation techniques, such as region growing from seed, and thresholding, ensuring that at least one method can perform well regardless of image conditions. This fail-safe methodology is particularly valuable for handling the broad spectrum of skin pigmentation, as current algorithms optimized for lighter skin tones, where skin to lesion contrast is typically higher [31], may fail or produce suboptimal results on darker skin.

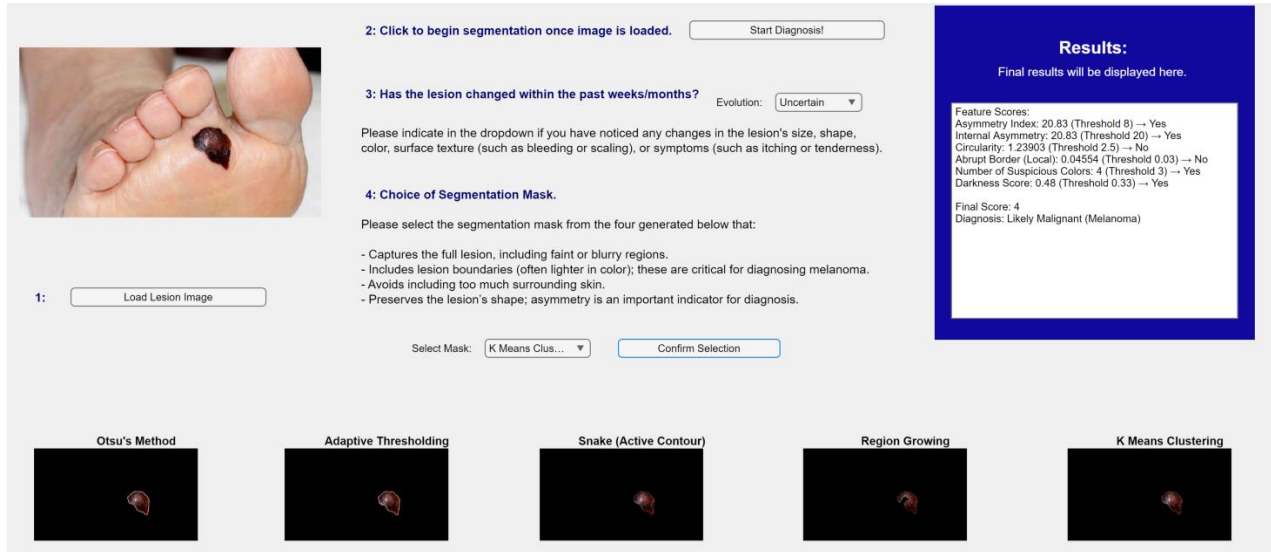
Once the optimal mask is selected, the system will automatically extract key morphological features from the lesion, namely asymmetry, border irregularity, color variation, and darkness, and use them to score the lesion using a modified ABCDE scale. Recognizing the limitations of diameter as a diagnostic feature, this work incorporates darkness as a critical substitute for the traditional criterion within the ABCDE framework. The final application will be designed to work with standard photographs taken under variable illumination without requiring dermoscopic imaging, making it suitable for both clinical and in-home use. By enabling reliable assessments outside of specialized facilities, the tool aims to encourage earlier medical consultations and intervention when warranted.

By combining multiple segmentation strategies with interactive mask selection, the project aims to mitigate errors when individual automatic methods fail, improving diagnostic reliability across diverse patient populations. It also bridges the gap between full automation and clinical judgment, enabling both clinicians and untrained users to make informed decisions before feature extraction and classification proceed, ultimately supporting earlier detection and intervention.

3. Methodology

For this project's implementation, a MATLAB App was developed for the user to load a lesion image, visualize the resulting masks side-by-side, select the optimal one, and immediately receive the diagnostic results (figure 1).

Figure 1. MATLAB Application UI for Melanoma Detection.



3.1. Preprocessing

In order to accurately analyze the lesion, it must be segmented from the surrounding skin in the image. This process can be made challenging due to image quality issues, namely illumination gradients caused by shadows and reflections on the skin, low resolution, and low contrast separating the lesion and background. Image artifacts, including the presence of hair and neighbouring skin marks, as well as random, "salt and pepper" noise, further threaten the segmentation accuracy. Therefore, the image must be preprocessed before segmentation in order to correct artifacts and enhance contrast as much as possible.

The various segmentation algorithms that are implemented in this application leverage different image characteristics. Intensity-based methods such as thresholding and active contour models primarily rely on grayscale intensity information to delineate lesion boundaries. In contrast, color-based algorithms like K-means clustering exploit chromatic information. This fundamental difference necessitated the design of two separate preprocessing pathways: one

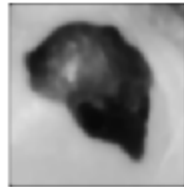
tailored to enhance grayscale intensity features for algorithms that depend on luminance, and another to process each color channel separately and prepare for color-based segmentation.

Unanimous to both preprocessing pathways, the first step prompts the user to manually trace an outline around the lesion boundary, directly on the input image using MATLAB's **drawfreehand** function. This manual delineation is particularly important for smartphone-acquired images, which are often zoomed out and include large amounts of surrounding skin. The freehand outline is converted into a binary mask, from which the bounding box of the traced region is computed using the **regionprops** function. The image and corresponding mask are cropped to this bounding box size. For standardization, the cropped image is resized to fit within a maximum size of 700 x 500 (8-bit RGB depth) while preserving its aspect ratio. This constraint ensures consistency across the dataset and reduces computational load during segmentation and feature extraction algorithms for very large images. This resizing is simultaneously applied to the corresponding ROI mask to maintain alignment.

3.1.1. Grayscale Preprocessing

For grayscale-dependent segmentation (figure 2), the cropped RGB input image is first converted to grayscale using MATLAB's **rgb2gray** function, which computes luminance via a weighted sum of the RGB channels.

Figure 2. Sample Preprocessed Grayscale Image.



3.1.1.1. Median Filtering

To eliminate impulse noise ("salt and pepper" pixels), and reduce hair artifacts, a median filter is applied to the grayscale image. **medfilt2** is the employed MATLAB command, which calculates, and assigns to each pixel, the median of the grey levels of its neighborhood. It was found empirically that setting a 5x5 neighborhood yielded optimal results. Median filtering was chosen over mean-based filtering because it is more robust to outliers in the neighborhood (for instance, a hair pixel) that would skew the local average.

3.1.1.2. Morphological Closing

Next, morphological closing is performed to ensure all hair artifacts are eliminated. The aim is to fill any narrow, dark gaps characteristic of hair streaks that may remain after median filtering. The grayscale, median-filtered image is processed using MATLAB's **imclose** function, which applies a dilation followed by erosion using a structuring element. A disk-shaped structuring element with radius 3 was chosen, based on recommendations from related works [17]. The dilation step bridges small black lines, and the erosion step restores the original structure, producing a smoothened, hair-free image.

3.1.1.3. Gaussian Smoothing

Finally, Gaussian smoothing is applied to remove high-frequency texture and subtle noise that may still interfere with segmentation algorithms. The smoothed image is computed using a 2D Gaussian filter created via MATLAB's **fspecial**('gaussian', ...), with standard deviation $\sigma = 1.2$ and a kernel size of 9×9 (rounded from the 6σ rule). This operation reduces small variations in skin texture and helps prevent the algorithm from mistaking noise or freckles for lesion boundaries.

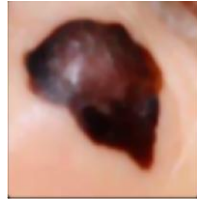
3.1.2. Color Preprocessing

Similar methodologies are used in the color preprocessing pathway, only applied to the separate color channels (figure 3). First, median filtering (**medfilt2**) is independently applied to each RGB channel with a 5×5 filter window, suppressing impulse noise and localized artifacts.

The filtered image is then transformed to the CIELab color space (**rgb2lab**) which approximates human visual perception and separates luminance (L^*) from chromaticity (a^* , b^*). Morphological closing is performed exclusively on the L^* channel using **imclose** with a disk-shaped structuring element of radius 3 to fill dark hair gaps while preserving all color integrity in a^* and b^* channels. The adjusted L^* channel is then recombined with the original chromatic channels and converted back to RGB (**lab2rgb**).

A final Gaussian smoothing step is applied independently to each RGB channel for generalized noise reduction. The same 2D Gaussian convolution filter is utilized, but with a smaller kernel size (4×4), and standard deviation $\sigma = 1.0$, to avoid blurring important color differences used for segmentation.

Figure 3. Sample Preprocessed Color Image.



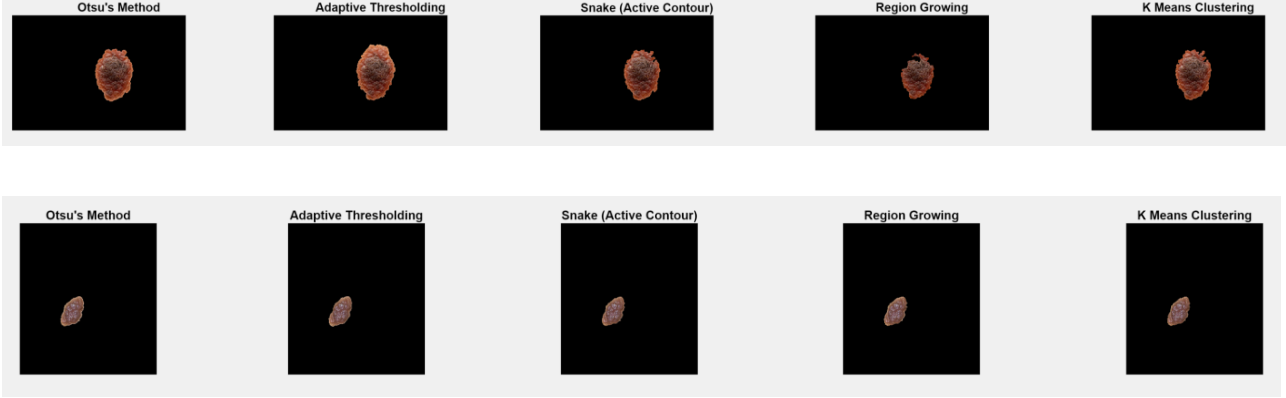
3.2. Segmentation

Binary image segmentation can be defined as the grouping of similar pixels into two distinct classes (i.e. lesion and non-lesion). In practice, this process can be made challenging due to image quality issues, such as illumination gradients, low lesion-skin contrast, irregular structural and color variations within lesions, the presence of hair and other artifacts, as well as the potential for multiple lesions within the same image [32, 33]. No single segmentation paradigm is universally optimal across all lesion presentations, which has motivated the use of a diverse set of algorithms that exploit different underlying principles [4]. In current dermatology applications, most segmentation methods are semi-automatic, requiring some interaction between the user and the software to achieve optimal results. This user involvement is not only acceptable, but can be advantageous, as it allows empirical selection of the most accurate segmentation when automatic methods produce variable outputs. In fact, Chang et al. [34] argued that it is impractical to perform fully automatic segmentation on all skin lesion images.

Given the heterogeneity of skin lesion images and the variety of challenges they present, this paper employs five distinct segmentation methods: Otsu's method, adaptive thresholding, active contour (Chan-Vese snake), seeded region growing, and K-means clustering in a perceptual-spatial feature space (figure 4). By generating multiple candidate masks and allowing the user to empirically select the most accurate result, the approach maximizes segmentation reliability while acknowledging the practical limitations of fully automated techniques.

Figure 4. Sample Image Segmentation Mask Results.





3.2.1. Basic Thresholding (Otsu's Method):

Otsu's method [18] is the simplest thresholding algorithm and particularly effective when the histogram exhibits a bimodal distribution corresponding to two well-defined intensity classes. Consider a grayscale image with L discrete gray levels $\{0, 1, 2, \dots, L-1\}$. The number of pixels at gray level i is denoted by n_i and the probability of occurrence of gray level i is:

$$p_i = \frac{n_i}{n}$$

Otsu's method partitions the image pixels into two classes: $C_0 = \{0, 1, \dots, T\}$ and $C_1 = \{T+1, T+2, \dots, L-1\}$. Then, the total probability for these two classes is $W_0(t) = \sum_{i=0}^T p_i$ for C_0 and $W_1(t) = \sum_{i=T+1}^{L-1} p_i$ for C_1 . The class means are computed from these distributions using the conditional probabilities: $\mu_0(T) = \frac{1}{W_0(T)} \sum_{i=0}^T i p_i$ and $\mu_1(T) = \frac{1}{W_1(T)} \sum_{i=T+1}^{L-1} i p_i$. Finally, the total mean gray level of the image is: $\mu_T(T) = \sum_{i=0}^{L-1} i p_i$.

The goal of Otsu's method is to find the optimal global threshold T^* that maximizes the between-class variance σ_b^2 between C_0 and C_1 :

$$\sigma_B^2 = W_0(\mu_0(T) - \mu_1(T))^2 + W_1(\mu_1(T) - \mu_T(T))^2$$

In this paper's MATLAB implementation, Otsu's method is applied by first normalizing the preprocessed grayscale image to the range $[0, 1]$. MATLAB's built-in function **graythresh** then computes the normalized threshold T^* by internally performing the above optimization over the image histogram. The image is binarized using **imbinarize** with the obtained threshold:

$$B(x, y) = \begin{cases} 1, & I(x, y) < T^* \\ 0, & \text{otherwise} \end{cases}$$

Since lesions typically appear darker than surrounding skin, the binary mask is then complemented to highlight the lesion region.

3.2.2. Adaptive Thresholding:

Unlike Otsu's method, which binarizes pixels based on one global threshold, adaptive thresholding improves segmentation generalizability by making use of local thresholds. This technique divides the image into overlapping blocks and calculates thresholds independently for each block, allowing the segmentation to adapt to local variations in intensity and texture across the lesion and surrounding skin.

The grayscale image of dimensions rows x cols is partitioned into overlapping blocks of size b x b, where the block size b is calculated as:

$$b = \text{round}(\min(0.07 \times \max(\text{rows}, \text{cols}), 0.5 \times \min(\text{rows}, \text{cols})))$$

with approximately 75% overlap between adjacent blocks, result in a step size of:

$$s = b - \text{overlap}, \quad \text{where } \text{overlap} \approx \frac{b}{1.3}$$

For each block B_{ij} , a local threshold T_{ij} is computed using Otsu's method (**graythresh** in MATLAB). The block is binarized accordingly with **imbinarize**. Assuming the lesion is darker than the surrounding skin, the binary block is complemented. These blocks are then aggregated into an accumulation map A and a weight map W, which count the sum of binarized pixels and the number of overlapping contributions per pixel, respectively. The final adaptive segmentation mask is derived by normalizing:

$$M = \left\{ x \mid \frac{A(x)}{W(x)} \right\} > 0.5$$

where pixels with average binarized value greater than 0.5 are classified as lesion.

3.2.3. Region Growing:

Region growing is a classical image segmentation technique that expands from a seed point by iteratively including neighboring pixels based on similarity criteria [26-28]. This method is particularly effective for segmenting lesions with relatively homogeneous color and texture properties in a perceptually uniform color space.

In this implementation, the input color image is first transformed into the CIE Lab color space because it better approximates human color perception. The region growing process begins from a seed, which is selected as the darkest pixel in the lesion area, automatically identified by the minimum L^* value within the user-drawn ROI bounding box.

The growth criterion is defined in a combined 5-dimensional feature space incorporating both color and spatial information: $f = [L^*, a^*, b^*, x, y]$. Feature weights are assigned empirically to balance the influence of each dimension.

At each iteration, the algorithm evaluates candidate neighboring pixels against two distance metrics: the distance to the mean feature vector of the current region f^{region} , and the distance to the seed pixel's feature vector, f^{seed} . These distances use the Euclidean metric weighted by the feature weights:

$$d_{region} = \sqrt{\sum_i w_i^2 (f_i^{candidate} - f_i^{region})^2}$$

$$d_{seed} = \sqrt{\sum_i w_i^2 (f_i^{candidate} - f_i^{seed})^2}$$

A pixel is added to the region if both distances fall below respective thresholds: a local threshold, $T_{region} = L_{tol}$, calculated adaptively as a multiple of the standard deviation of the L^* channel, and a global threshold, $T_{seed} = 1.5 \times L_{tol}$. This dual thresholding ensures that pixels are similar both to the evolving region and the original seed, improving robustness to local intensity variations and preventing leakage into dissimilar areas.

The iterative procedure continues by exploring the 8-connected neighbourhood of accepted pixels, updating the region mean feature vector dynamically. A maximum allowed number of consecutive “too bright” pixels in any direction is set to prevent premature termination due to glare or other artifacts related to overexposure.

3.2.4. Active Contour (Snake):

Active contour models, commonly referred to as “snakes” [16, 29], are inherently region-based segmentation methods that function by iteratively evolving a contour to fit object boundaries. This implementation uses the Chan-Vese model, which is particularly effective for segmenting objects with poorly defined edges or heterogeneous intensity.

Given a grayscale image I and an initial mask that approximates the lesion location, the goal is to iteratively update the contour to minimize an energy “cost” function. This function is comprised of internal energy terms, which depend on the shape of the contour only to penalize jagged or implausible contours, and external energy terms, which depend on the image edges and

intensities to penalize inaccurate contours. The curve evolution proceeds for a specified number of iterations. Since larger images require a greater number of iterations for convergence, the number of iterations is dynamically scaled with image size, calculated as:

$$N = \min(1500, \text{round}(190 + 0.005 \times \text{rows} \times \text{cols}))$$

The snake-based lesion mask is acquired in MATLAB using the built-in **activecontour** function, which takes the preprocessed grayscale image, the initial binary mask and the number of iterations as inputs. This approach enables accurate lesion boundary delineation even in cases of low contrast or blurred edges.

3.2.5. K Means Clustering:

K-means clustering is a type of unsupervised machine learning algorithm that partitions image pixels into a predefined number of clusters based on similarity in a combined color-spatial feature space [23, 24]. In this implementation, each pixel is described by a five-dimensional feature vector: $f = [L^*, a^*, b^*, y, x]$.

To balance the influence of different feature dimensions, each component is normalized to $[0, 1]$ and scaled by empirically determined weights, W .

$$L = \frac{L^*}{100} W_L, \quad a = \frac{a^* + 128}{255} W_a, \quad b = \frac{b^* + 128}{255} W_b$$

$$y = \frac{y}{\max(y)} W_s, \quad x = \frac{x}{\max(x)} W_s$$

Higher priority ($W_L = 6.99$) is assigned to lightness to exploit the common observation that melanocytic lesions are darker than surrounding skin, while moderate weights ($W_a = W_b = 0.5$) are given to chromatic axes and a low-medium weight to spatial terms ($W_s = 1.48$) to discourage fragmented, non-compact clusters. The resulting design emphasizes perceptual separation in $L^*a^*b^*$ while gently biasing clusters to be spatially coherent.

Clustering proceeds with k randomly initialized centroids in the feature space (here $k = 3$). It then iteratively alternates between assigning each pixel to its nearest centroid using the squared Euclidean distance,

$$d_{ij} = \|f_i - \mu_j\|_2^2$$

and updating each centroid μ_j as the mean of the pixels assigned to it. The total clustering cost, or objective function, is computed at each iteration:

$$J(\{\mu_j\}) = \sum_{i=1}^N \sum_{j=1}^k r_{ij} \|f_i - \mu_j\|_2^2$$

Where $r_{ij} \in \{0,1\}$ indicates the assignment of pixel i to cluster j , and μ_j is the centroid of cluster j . Assignment and centroid update steps continue to alternate until the change in J falls below a convergence threshold. These steps are implemented explicitly with a responsibility matrix $R = r_{ij}$ and the cost history J to monitor convergence.

After convergence, each pixel is assigned to its closest centroid. Because melanomas typically occupy the darkest mode in L^* , the lesion is selected as the cluster with the minimum median L^* among the k clusters, yielding the desired binary mask.

3.3. Morphological Post Processing

Following initial mask generation, each segmentation method undergoes a post-processing stage designed to produce a clean and continuous lesion representation. This stage relies on morphological operations to address typical segmentation imperfections in the mask, such as disconnected regions, small non-lesion clusters that were retained, narrow background gaps and holes scattered within the mask boundaries. The post-processing implementation details are tuned to the unique characteristics of each segmentation algorithm.

In all cases, the first step is to ensure that only the primary cluster is retained (i.e., the lesion cluster). Because melanoma images generally contain a geographically continuous lesion of interest, the largest connected component is isolated using area-based filtering (**bwareafilt**), which removes smaller, unrelated objects. This is followed by a process of sealing narrow canals between the lesion and the surrounding skin, either through morphological closing (**imclose**) or targeted conversion of thin background strips to foreground. The latter method is based on the Euclidean distance transform. A distance map (**bwdist**) is computed for the binary mask, measuring for each background pixel its nearest distance to the lesion boundary. Background pixels whose distance is less than or equal to a small threshold (e.g., $t = 3$ pixels) are reclassified as lesion, effectively “painting in” narrow strips that cause fragmentation if left unfilled. Once these discontinuities are bridged using either method, any fully enclosed background regions are treated as internal holes and filled using the **imfill** command, to create a solid lesion region. Finally, small residual specks are removed based on area thresholds.

Although this framework is applied consistently across all segmented masks, the degree of smoothing, the structuring element sizes, and the operation order vary. For K-means clustering, which selects the darkest cluster as the lesion, the resultant mask often contains internal holes or fragmented patches. To address this, morphological closing is applied with a structuring element whose radius is adaptive to the scale of the user-scaled image ROI. The goal is to ensure that the closing operation can bridge gaps that are proportionally small relative to the lesion size, while avoiding excessive dilation that could merge the lesion with surrounding skin. The radius r is defined as:

$$r = \max(1, \text{round}(\frac{\min(H, W)}{300}))$$

where W and H are the width and height of the cropped image, in pixels. The structuring element is a disk, created in MATLAB using `strel('disk', r)` which performs isotropic closing without bias toward any direction. After this adaptive closing step, the mask is processed to **imfill** to fill any remaining enclosed voids and then lightly opened (**imopen**) to remove the minor overgrowth along edges that closing can introduce.

For Otsu's method, which often yields relatively sharp lesion boundaries for high-contrast, bimodal images, only a mild closing is applied to avoid altering fine edge details, preceded by the targeted narrow-gap sealing procedure (using **bwdist**), and followed by light speck removal. Adaptive thresholding, in contrast, tends to produce boundary variability between local blocks. Hence, smoothing plays a more prominent role, and slightly more aggressive speck removal is applied to suppress block-based artifacts, the rest of the steps remaining the same. Active contour (snake) segmentation inherently produces smoother, topologically consistent boundaries, thus minimal post-processing is required. Small radius closing and light opening are sufficient to regularize edges. Finally, region growing outputs can include jagged or uneven perimeters, particularly in areas of gradual intensity change. Therefore, these masks benefit from earlier hole filling, a larger closing radius to smooth the boundary, and a subsequent opening to remove edge debris.

3.4. Feature Extraction

3.4.1. Asymmetry (A)

Asymmetry assessment begins with spatial standardization of the lesion mask. The image is first cropped to its bounding box as per the user-drawn ROI. Using region properties computed via MATLAB's **regionprops** function, the lesion's centroid and principal axis orientation are determined. To ensure uniformity in analysis and comparability across images, the lesion is then translated so that its centroid coincides with the geometric center of the bounding box, and rotated to align the major axis horizontally.

Mathematically, the asymmetry index (AI) is computed by comparing the lesion mask to its flipped versions along both the horizontal and vertical axes. Let M denote the aligned binary lesion mask, M_H the horizontally flipped mask (via MATLAB's **fliplr**), and M_V the vertically flipped mask (via MATLAB's **flipud**). The non-overlapping regions between the original and flipped masks are quantified by the pixel-wise XOR operation:

$$D_H = M \oplus M_H, \quad D_V = M \oplus M_V$$

The number of pixels differing between the masks is calculated using **nnz** (number of non-zero elements). The asymmetry indices for each axis are defined as the ratios of these differing pixel counts normalized to the lesion area A :

$$AI_H = \frac{\sum D_H}{A}, \quad AI_V = \frac{\sum D_V}{A}$$

The final asymmetry index is the average of these two measures, scaled to percentage form.

$$AI = 100 \frac{AI_H + AI_V}{2}$$

3.4.2. Border Irregularity (B)

To quantify border irregularity, two complementary metrics were employed: a global circularity measure and a local edge complexity score. The first metric, circularity, serves as a classical shape descriptor defined mathematically as:

$$C = \frac{P^2}{4\pi A}$$

where P represents the perimeter of the lesion and A is the lesion's area. MATLAB's **regionprops** command is used to calculate the area and perimeter of the lesion mask with sub-

pixel precision. The circularity metric attains a minimum value of 1 for a perfect circle and increases as the lesion boundary deviates from this ideal smooth shape, thereby providing a global measure of border irregularity. Lesions with higher circularity values are indicative of more complex, uneven borders.

In parallel, the Sobel edge-based boundary density metric is used to quantify the relative abundance of edge pixels detected on the lesion mask normalized by the lesion area. The Sobel operator is a gradient-based edge detector that highlights areas of rapid intensity change, thus emphasizing boundary transitions in the binary lesion mask. This metric is computed as:

$$B = \frac{\sum \text{edge pixels}}{\sum \text{lesion pixels}}$$

MATLAB's **edge** command is used to count the number of pixels identifies as edges by the Sobel filter. The number of lesion pixels is determined by the total number of pixels within the lesion mask. This measure reflects the local complexity of the lesion border, capturing fine-scale irregularities and micro-boundary features that may not significantly affect the global perimeter. Utilizing both metrics enhances the border irregularity assessment by integrating both macro- and micro-structural lesion border characteristics.

3.4.3. - Colour Variation (C)

As opposed to pigmented benign lesions which tend to be uniform, melanoma generally contains more than two distinct colors. Importantly, based on the CASH algorithm developed by Henning et al. in 2008, melanocytic lesions often include one or more of the following six suspicious shades of color: white, red, light brown, dark brown, blue-gray, and black [35]. Therefore, the presence of these colors in the skin lesion image must be quantified for melanocytic assessment.

To measure the number of perceptually distinct colors within the lesion, this analysis leverages the CIELab color space, which approximates human color perception more accurately than the RGB space. The lesion pixels are first isolated using the segmentation mask applied to the original RGB image. These pixels are then converted from RGB to CIELab using MATLAB's **rgb2lab** function.

Color clustering is performed using MATLAB's **kmeans** function, which partitions the lesion pixels into $k = 7$ color clusters, corresponding to the six suspicious melanoma colors. The six suspicious colors are predefined as follows based on the literature [35]:

- Black: $L^* \in [0.06, 39.91]$, $a^* \in [0.27, 30.23]$, $b^* \in [0.10, 22.10]$
- Dark Brown: $L^* \in [14.32, 47.57]$, $a^* \in [6.85, 27.14]$, $b^* \in [6.96, 46.81]$
- Light Brown: $L^* \in [47.94, 71.65]$, $a^* \in [11.89, 44.81]$, $b^* \in [19.86, 64.78]$
- White: $L^* = 100$, $a^* = 0$, $b^* = 0$ (single point)
- Red: $L^* = 54.29$, $a^* = 80.81$, $b^* = 69.89$ (single point)
- Blue Gray: $L^* = 50.28$, $a^* = -30.14$, $b^* = -11.96$ (single point)

The kmeans function operates by initializing cluster centroids and iteratively assigning pixels to the nearest centroid based on Euclidean distance, then recalculating centroids until convergence. To avoid overcounting subtle shade variations as separate colors, clusters that are close in chromaticity (measured by Euclidean distance between centroids in the a^*b^* plane), are merged.

Each cluster centroid is compared to the reference suspicious colors using Minkowski distance of order $p = 3$ as a generalized metric for perceptual similarity. The Minkowski distance between two color vectors x and y in CIELab space is defined as:

$$d_m(x, y) = \left(\sum_{i=1}^3 |x_i - y_i|^p \right)^{1/p}$$

For white, red and blue gray (single point colors), the cluster is considered matching if:

$$d_m(\text{centroid}, \text{reference}) < T$$

where T is a threshold computed as half the Minkowski distance between the white and black reference colors ($T = \frac{1}{2} d_m(L_{\text{white}}, L_{\text{black}})$).

For the range-based colors (black, dark brown, light brown), the centroid's components must lie within the defined minimum and maximum bounds for L^* , a^* and b^* simultaneously to be classified as that color.

Additionally, a cluster's presence is only considered significant if it contains at least 5% of total lesion pixels. This approach yields a robust estimate of the number of suspicious colors within the lesion.

3.4.4. Darkness (D)

The algorithm adopts a modernized approach to the ABCDE rule by replacing ‘Diameter’ with ‘Darkness’ as a critical feature for melanoma detection. This shift reflects evidence that darkness is a sensitive marker, particularly for early melanomas that have not yet reached large sizes [14, 15].

Lesion darkness is quantified relative to the patient’s surrounding skin to account for variability in baseline skin tones across individuals. The original RGB image is converted to CIELab color space to obtain luminance L^* values for each pixel. Mean luminance values are computed separately for lesion pixels (using the segmentation mask) and background skin pixels (the complement of the lesion mask). The darkness score is calculated as the normalized difference between the background and lesion means:

$$\text{Darkness Score} = \max \left(0, \frac{\bar{L}_{\text{background}} - \bar{L}_{\text{lesion}}}{100} \right)$$

Since L^* ranges approximately from 0 (black) to 100 (white), normalizing by 100 ensures the score ranges between 0 and 1, with higher values indicating a lesion darker than the surrounding skin.

3.4.5. Evolution (E)

The algorithm incorporates lesion evolution as an optional but clinically important feature in melanoma assessment. Evolution refers to changes in a lesion over time, including variations in size, shape, color, surface characteristics, or symptoms such as itching or bleeding [10]. The system allows the user to input an evolution status through a dropdown selection with three possible values “Yes,” “No,” or “Uncertain.” These choices correspond to a discrete numerical score, E , assigned as follows:

$$f(x) = \begin{cases} +1, & \text{if lesion evolution is present ('Yes')} \\ 0, & \text{if evolution is uncertain ('Uncertain')} \\ -1, & \text{if no evolution is reported ('No')} \end{cases}$$

3.5. Classification

The final lesion classification is computed using a weighted scoring system inspired by the ABC-point list approach, which simplifies the traditional ABCDE criteria by converting each diagnostic feature into a binary score, either 0 or 1, based on whether the lesion exceeds clinically defined thresholds. This binary framework contrasts with purely numeric scoring as seen with traditional ABCD scales, providing greater robustness against measurement variability [7, 8].

In this algorithm, each extracted feature, being asymmetry, border irregularity, color variation, darkness, and evolution, is compared against empirically derived thresholds. If the measurement surpasses its respective threshold, the feature is assigned a value of 1, indicating suspicion, otherwise 0.

Among these features, color variation ('C') is considered the earliest sign of melanoma and has a high predictability for the diagnosis of the disease. In fact, studies have demonstrated that color variation might be the most important singular discriminator of melanoma [36]. For this reason, the 'C' score is attributed a greater weight of 1.5 in the scoring formula. The recognized threshold for melanoma is three or more of the suspicious colors [35]. In contrast, pigmentation intensity, quantified as darkness relative to surrounding skin, is weighted conservatively at 0.5, to reflect the fact that it is a relatively novel, unestablished ABCDE criterion, that faces some scrutiny in cases of lighter melanoma with more pink-red hues [37]. The empirical threshold for the quantified darkness score is set to 0.4.

Asymmetry is evaluated using two discrete thresholds to capture varying degrees of lesion irregularity. The first threshold, empirically set to an AI value of 7, serves as a baseline indicator, marking lesions that exhibit noticeable asymmetry, which is a common hallmark of early malignant change [38]. Lesions exceeding this threshold contribute one point to the total diagnostic score. To identify lesions with particularly pronounced asymmetry, a second, higher threshold at an AI value of 14 is applied. Exceeding this threshold signifies severe asymmetry, suggesting an even more likely positive diagnosis. When this occurs, an additional point is added to the diagnostic score. This dual-threshold approach aligns with clinical observations that greater asymmetry correlates strongly with melanoma malignancy [36, 38].

Finally, the border irregularity score is broken down into two components, local and global. The more traditional, global measure is weighted at 0.75, while the local measure is

weighted at 0.5. This ensures border irregularity metrics are not overemphasized in the calculation despite a dual presence of contributing factors.

The total diagnostic score (TDS) is then calculated as:

$$TDS = A_{lower} + A_{upper} + 0.75 B_{circularity} + 0.5 B_{local} + 1.5 C + 0.5 D + E$$

Classification logic is applied to categorize the lesion into one of three diagnostic groups: “Likely Malignant (Melanoma)” for scores of 4.0 or higher, “Suspicious: Needs Dermatologist Review” for scores between 2.5 and 4.0, and “Likely Benign” for scores below 2.5. This tiered structure prioritizes user safety by ensuring that any lesion with a high likelihood of malignancy is flagged for urgent follow-up, while also identifying uncertain cases that warrant further investigation. The thresholds are chosen to maximize sensitivity, because missing a malignant lesion (false negative) poses a far greater clinical risk than misclassifying a benign lesion as suspicious (false positive).

3.6. Evaluation of System Performance

To evaluate the performance of the segmentation and scoring system, a dataset of manually labeled images was processed using the five implemented segmentation methods: Otsu thresholding (‘Otsu’), adaptive thresholding (‘AT’), active contour (‘Snake’), region growing (‘RG’) and K-means clustering (‘K means’). Each image was assigned a ground-truth classification label – positive melanoma (P), negative melanoma as a mole (N), or negative melanoma as another type of benign lesion (O). In total, the dataset contained 40 images of malignant melanoma (P), 23 images of moles (N) and 8 images of other lesions (O). The images were manually curated from a variety of sources, listed in the references section. They span a variety of angles, camera qualities, and levels of zoom, as well as a wide range of skin tones, lesion shapes, and color variations. This diversity was critical to assessing the robustness of the program under the variability that a real-world diagnostic tool would encounter.

For each image, all five segmentation algorithms were executed in the MATLAB app, and their masks were visually reviewed. The best mask for that image was manually selected, and the diagnostic score was computed. The following performance metrics were recorded for each image in the dataset (table 1):

- **Raw scores for each method:** A manually assigned 0-3 score indicating the mask's quality for each segmentation method. Masks that score a 0 fail entirely, 1 is satisfactory, 2 is good and 3 is ideal.
- **Number of successes:** The count of algorithms achieving an acceptable segmentation (nonzero score) for a given image.
- **Best mask selection:** The segmentation algorithm chosen.
- **Final diagnostic score:** the TDS score for the best mask.

True positives (TP), true negatives (TN), false positives (FP), and false negatives (FN) were determined according to the app's internal classification thresholds. False negatives were defined as cases where the ground truth is positive melanoma, and the score is below 2.0. False positives were defined as cases where the ground truth is negative, and the score is 4.0 or above.

Table 1. Sample Recorded Data.

	Otsu	AT	Snake	RG	K Means	# successes	Best Mask	Score for best mask	Image Characteristics
P	3	3	2	1	2	5	AT	5.5	white skin, high contrast, well-defined boundaries
P	2	3	2	0	2	4	AT	3.5	white skin, high contrast
P	3	1	2	1	2	5	Otsu	4.5	white skin, high contrast, high colour variation
P	3	1	3	2	3	5	Otsu	3.5	white skin, high contrast, low colour variation
P	3	3	3	3	3	5	Otsu	4.5	white skin, ill-defined boundaries, low colour variation, high contrast
P	3	3	2	2	3	5	AT	4.5	white skin, high contrast, low colour variation

4. Results

The summary statistics table (table 2) shows average diagnostic scores grouped by case type (P, N, O), the number of times each method was chosen as the best mask, the average raw score per method, and classification metrics such as sensitivity, specificity, false positive rate (FPR) and false negative rate (FNR). Overall, the system exhibited a sensitivity a 94.87% and specificity of 93.33%, indicating that both false positives (n=2) and false negatives (n=2) were rare. The low relatively low FPR (6.67%) and FNR (5.13%) confirm that the threshold and scoring method provide basic diagnostic accuracy. The low FNR is particularly important for melanoma detection, as missing a malignant lesion poses a significantly grater clinical risk than over-calling a benign lesion. The low FPR reduces unnecessary follow-up burden.

Table 2.

Summary Statistics	<i>Otsu</i>	<i>AT</i>	<i>Snake</i>	<i>RG</i>	<i>K Means</i>
Average score for P cases	4.038462				
Average score for N cases	2.23913				
Average score for O cases	3.428571				
False positives (FP)	2				
False negatives (FN)	2				
True positives (TP)	37				
True negatives (TN)	28				
Count of times each mask type is best	30	11	5	8	15
Average for each method's raw score	2.26087	1.246377	2	1.405797	2.072464
Average # successes for P cases	3.846154				
Average # successes for N cases	4.521739				
Average # successes for O cases	2.428571				
Sensitivity	0.948718				
Specificity	0.933333				
False positive rate	0.066667				
False negative rate	0.051282				

4.1. Performance Across Case Types

Average diagnostic scores reflected clear separation between malignant and benign pigmented lesions. Melanoma cases averaged 4.04, comfortably above the malignancy threshold

(4.0), while benign moles averaged 2.24, below the benign classification cutoff (2.5). The “other” benign lesion group averaged 3.43, higher than moles, likely because certain lesion types share structural and color characteristics with melanoma. These results underscore the importance of developing additional discriminatory features to avoid misclassification of non-melanoma pigmented lesions.

In terms of segmentation accuracy, benign moles (N) had the highest number of successful masks per image (4.52). P cases performed second best, with 3.85 successful masks per image, and O cases had 2.43. The higher success rate in N cases may be due to the typically higher contrast and smoother boundaries of benign moles, while some O cases (e.g., seborrheic keratoses) present with irregular texture and colors that confuse the algorithms that rely on simpler feature distributions.

4.2. Segmentation Method Comparison

When examining raw scores across all images, Otsu had the highest number of best mask selections (30 cases), followed by K-means (15 cases) and adaptive thresholding (11 cases). Region growing and snake algorithms were selected frequently, at 8 and 5 cases respectively. The average raw score per method reveals a similar leaderboard: Otsu (2.26) and K-means (2.07) attaining the highest scores, with Snake (2.00), RG (1.41) and AT (1.25) trailing. The variability in best-mask selections confirms that no single algorithm universally outperforms others.

Interestingly, although Region Growing was not a top overall performer, it empirically yielded the best results on darker skin tones. This is likely because its pixel-by-pixel expansion from a seed point relies more on local color and intensity similarity than on global contrast, making it less prone to misclassification when lesion and background share a narrow overall luminance range.

5. Conclusion

Malignant melanoma is a life-threatening dermatological disease whose prognosis depends critically on early detection. In this work, a novel diagnostic pipeline was developed that integrates multiple image processing algorithms, feature extraction, and classification techniques to assist in melanoma detection. Five independent segmentation methods, being Otsu, adaptive thresholding, active contour modelling, region growing, and K-Means, were implemented to provide diverse candidate lesion masks. Clinically relevant features were extracted from the optimal, user-selected mask, including asymmetry index, border abruptness, circularity, darkness relative to surrounding skin, and the presence of suspicious colors. These features were used to produce a diagnostic likelihood score inspired by the ABC-point list criteria for melanoma detection.

While the results show the system can successfully identify and quantify diagnostic features, the image dataset used for testing was entirely manually collected and small, containing only 71 images. As a result, accuracy, sensitivity, specificity and overall generalizability remain uncertain. Additionally, the current workflow relies heavily on user interaction, which limits scalability in research or other large-scale screening contexts.

Future work should address these limitations. First, the system must be validated on a substantially larger and more diverse dataset. Second, the level of user interaction could be reduced. Machine learning models could be trained to evaluate the quality of each candidate mask based on predefined desirable characteristics (e.g., shape continuity, blob-like geometry, lesion-skin contrast, absence of mask pixels on image edges). The optimal mask could then be selected without user input. Similarly, the final score calculation could be automated and optimized by a learning algorithm trained on a large, labeled dataset, allowing the system to determine the most predictive weighting of extracted features for melanoma detection. These improvements would allow for a fully automated pipeline that improves and generalizes seamlessly as more data is introduced over time.

6. References

- [1] Argenziano, G., Soyer, H., De Giorgi, V., et al. (2000). *Interactive atlas of dermoscopy* (Book and CD-ROM). Milano, Italy: Edra Medical Publishing and New Media.
- [2] Satheesha, T. Y., Satyanarayana, D., Prasad, M. N. G., & Dhruve, K. D. (2017). Melanoma is skin deep: A 3D reconstruction technique for computerized dermoscopic skin lesion classification. *IEEE Journal of Translational Engineering in Health and Medicine*, 5, 1–17.
<https://doi.org/10.1109/JTEHM.2017.2648797>
- [3] Zebari, N. A. M. (2022). *Skin cancer diagnosis based on machine learning techniques* (Master's thesis, Harran University).
- [4] Celebi, M. E., Aslandogan, Y. A., & Bergstresser, P. R. (2005). Unsupervised border detection of skin lesion images. *International Conference on Information Technology: Coding and Computing (ITCC)*.
<https://doi.org/10.1109/ITCC.2005.283>
- [5] Stolz, W. (1994). ABCD rule of dermatoscopy: A new practical method for early recognition of malignant melanoma. *European Journal of Dermatology*, 4, 521–527.
<https://cir.nii.ac.jp/crid/1571417125204517120>
- [6] Nachbar, F., Stolz, W., Merkle, T., Cagnetta, A. B., Vogt, T., Landthaler, M., et al. (1994). The ABCD rule of dermatoscopy: High prospective value in the diagnosis of doubtful melanocytic skin lesions. *Journal of the American Academy of Dermatology*, 30(4), 551–559.
[https://doi.org/10.1016/S0190-9622\(94\)70061-3](https://doi.org/10.1016/S0190-9622(94)70061-3)
- [7] Blum, A., Rassner, G., & Garbe, C. (2003). Modified ABC-point list of dermoscopy: A simplified and highly accurate dermoscopic algorithm for the diagnosis of cutaneous melanocytic lesions. *Journal of the American Academy of Dermatology*, 48(5), 672–678. <https://doi.org/10.1067/mjd.2003.282>
- [8] Meo, N. D., Stinco, G., Bonin, S., Gatti, A., Trevisini, S., Damiani, G., et al. (2015). CASH algorithm versus 3-point checklist and its modified version in evaluation of melanocytic pigmented skin lesions: The 4-point checklist. *Journal of Dermatology*, 42.
- [9] Kanimozhi, T., & Murthi, A. (2016). Computer aided melanoma skin cancer detection using artificial neural network classifier. *SJSR*.
- [10] Abbasi, N. R., Shaw, H. M., Rigel, D. S., et al. (2004). Early diagnosis of cutaneous melanoma: Revisiting the ABCD criteria. *JAMA*, 292(22), 2771–2776. <https://doi.org/10.1001/jama.292.22.2771>
- [11] Liu, W., Hill, D., Gibbs, A. F., Tempany, M., Howe, C., Borland, R., et al. (2005). What features do patients notice that help to distinguish between benign pigmented lesions and melanomas? The ABCD(E) rule versus the seven-point checklist. *Melanoma Research*, 15(6), 549–554.
<https://doi.org/10.1097/00008390-200512000-00011>
- [12] International Skin Imaging Collaboration. SIIM-ISIC 2020 Challenge Dataset. *International Skin Imaging Collaboration* <https://doi.org/10.34970/2020-ds01> (2020)
- [13] Shaw, H. M., & McCarthy, W. H. (1992). Small-diameter malignant melanoma: A common diagnosis in New South Wales, Australia. *Journal of the American Academy of Dermatology*, 27(5), 679–682.
- [14] Goldsmith, S. M. (2021). Why is darkness an essential feature for melanoma recognition? *Skinmed*, 19(5), 334–336.
- [15] Ferrari, C., Seidenari, S., Borsari, S., et al. (2014). Dermoscopy of small melanomas: Just a miniaturized dermoscopy? *British Journal of Dermatology*. <https://doi.org/10.1111/bjd.12542>
- [16] Okuboyejo, D. A., & Olugbara, O. O. (2018). A review of prevalent methods for automatic skin lesion diagnosis. *The Open Dermatology Journal*, 12, 14–53.
<https://doi.org/10.2174/187437220181201014>
- [17] Smaoui, N., & Bessassi, S. (2013). A developed system for melanoma diagnosis. *International Journal of Computer Vision and Signal Processing*, 3(1), 10–17.
- [18] Otsu, N. (1979). A threshold selection method from gray level histogram. *IEEE Transactions on Systems, Man, and Cybernetics*, 9(1), 62–66. <https://doi.org/10.1109/TSMC.1979.4310076>

- [19] Premaladha, J., Priya, M. L., Sujitha, S., & Ravichandran, K. S. (2015). Normalised Otsu's segmentation. *Indian Journal of Science and Technology*, 8(22), 1–6.
<https://doi.org/10.17485/ijst/2015/v8i22/79140>
- [20] Mendonça, T., Marçal, A. R. S., Vieira, A., Nascimento, J. C., Silveira, M., Marques, J. S., et al. (2007). Comparison of segmentation methods for automatic diagnosis of dermoscopy images. *Conference of the IEEE Engineering in Medicine and Biology Society (EMBS)*, 6572–6575.
<https://doi.org/10.1109/IEMBS.2007.4353865>
- [21] Silveira, M., Nascimento, J. C., Marques, J. S., Marçal, A. R. S., Mendonça, T., Yamauchi, S., et al. (2009). Comparison of segmentation methods for melanoma diagnosis in dermoscopy images. *IEEE Journal of Selected Topics in Signal Processing*, 3(1), 35–45.
<https://doi.org/10.1109/JSTSP.2008.2011119>
- [22] Norton, K.-A., Iyatomi, H., Celebi, M. E., Schaefer, G., Tanaka, M., & Ogawa, K. (2010). Development of a novel border detection method for melanocytic and non-melanocytic dermoscopy images. *32nd Annual International Conference of the IEEE EMBS*.
<https://doi.org/10.1109/IEMBS.2010.5626499>
- [23] Liu, Z., Sun, J., Smith, M., Smith, L., & Warr, R. (2012). Unsupervised sub-segmentation for pigmented skin lesions. *Skin Research and Technology*, 18(1), 77–87. <https://doi.org/10.1111/j.1600-0846.2011.00534.x>
- [24] Zhou, H., Chen, M., Zou, L., Gass, R., Ferris, L., & Drogowski, L., et al. (n.d.). Spatially constrained segmentation of dermoscopy images. *International Symposium on Biomedical Imaging (ISBI)*.
- [25] Zhou, H., Rehg, J. M., & Chen, M. (2010). Exemplar-based segmentation of pigmented skin lesions from dermoscopy images. *International Symposium on Biomedical Imaging (ISBI)*.
<https://doi.org/10.1109/ISBI.2010.5490372>
- [26] Cavalcanti, P. G., & Scharcanski, J. (2013). A coarse-to-fine approach for segmenting melanocytic skin lesions in standard camera images. *Computer Methods and Programs in Biomedicine*, 112(3), 684–693. <https://doi.org/10.1016/j.cmpb.2013.08.010>
- [27] Mary, M., Padma, L., & John, M. (2014). Modified image segmentation method based on region growing and region merging. Faculty of Electronics and Communication Engineering, Noorul Islam University.
- [28] Pennisi, A., Bloisi, D. D., Nardi, D., Giampetruzzi, A. R., Mondino, C., & Facchiano, A. (2016). Skin lesion image segmentation using Delaunay triangulation for melanoma detection. *Computerized Medical Imaging and Graphics*, 52, 89–103. <https://doi.org/10.1016/j.compmedimag.2016.05.002>
- [29] Mete, M., & Sirakov, N. M. (2010). Lesion detection in dermoscopy images with novel density-based and active contour approaches. *BMC Bioinformatics*, 11(Suppl. 6), S23.
<https://doi.org/10.1186/1471-2105-11-S6-S23>
- [30] Chan, T. F., Sandberg, B. Y., & Vese, L. A. (2000). Active contours without edges for vector-valued images. *Journal of Visual Communication and Image Representation*, 11(2), 130–141.
<https://doi.org/10.1006/jvci.1999.0442>
- [31] University of New Mexico School of Medicine. (2023). Inclusive dermatology: Creating a diverse visual atlas of skin conditions. Retrieved February 23, 2023, from <https://hsc.unm.edu/medicine/departments/dermatology/inclusive-dermatology/>
- [32] Abbas, Q., Fondón, I., & Rashid, M. (2011). Unsupervised skin lesions border detection via two-dimensional image analysis. *Computer Methods and Programs in Biomedicine*, 104(3), e1–e15.
<https://doi.org/10.1016/j.cmpb.2011.07.008>
- [33] Cudek, P., Grzymala-Busse, J. W., & Hippe, Z. W. (2010). Melanocytic skin lesion image classification. Part I: Recognition of skin lesion. *International Conference on Human System Interactions (HSI)*, Rzeszow, Poland.
- [34] Chang, W.-Y., Huang, A., Chen, Y.-C., et al. (2015). The feasibility of using manual segmentation in a multifeature computer-aided diagnosis system for classification of skin lesions: A retrospective comparative study. *BMJ Open*, 5(4), e007823. <https://doi.org/10.1136/bmjopen-2015-007823>

- [35] Henning, J. S., Dusza, S. W., Wang, S. Q., Marghoob, A. A., Rabinovitz, H. S., Polsky, D., & Kopf, A. W. (2007). The CASH (color, architecture, symmetry, and homogeneity) algorithm for dermoscopy. *Journal of the American Academy of Dermatology*, 56(1), 45–52. <https://doi.org/10.1016/j.jaad.2006.09.003>
- [36] Ali, A. R., Li, J., & O'Shea, S. J. (2020). Towards the automatic detection of skin lesion shape asymmetry, color variegation and diameter in dermoscopic images. *PLOS ONE*, 15(6), e0234352. <https://doi.org/10.1371/journal.pone.0234352>
- [37] Rader, R. K., Payne, K. S., Guntupalli, U., Rabinovitz, H. S., Oliviero, M. C., Drugge, R. J., Malter, J. J., & Stoecker, W. V. (2014). The pink rim sign: Location of pink as an indicator of melanoma in dermoscopic images. *Journal of Skin Cancer*, 2014, 719740. <https://doi.org/10.1155/2014/719740>
- [38] Ruela, M., Barata, C., Marques, J. S., & Rozeira, J. (2017). A system for the detection of melanomas in dermoscopy images using shape and symmetry features. *Computer Methods in Biomechanics and Biomedical Engineering: Imaging & Visualization*, 5(2), 127–137. <https://doi.org/10.1080/21681163.2015.1029080>

6.1. Image References.

Melanoma1.jpg Courtesy of: <https://en.wikipedia.org/wiki/Melanoma>

Melanoma2.jpg Courtesy of: <https://health.clevelandclinic.org/how-to-spot-cancerous-moles/>

Melanoma3.jpg Courtesy of: ISIC

Melanoma4.jpg Courtesy of: ISIC

Melanoma5.jpg Courtesy of: ISIC

Melanoma6.jpg Courtesy of: <https://www.shutterstock.com/search/melanoma>

Melanoma7.jpg Courtesy of: CDSS

Melanoma8.jpg Courtesy of: ISIC

Melanoma9.jpg Courtesy of: ISIC

Melanoma10.jpg Courtesy of: <https://walkindermatology.com/patient-education/melanoma/>

Melanoma11.jpg Courtesy of: <https://www.health.com/condition/melanoma/is-it-a-mole-or-skin-cancer>

Melanoma12.jpg Courtesy of: ISIC

Melanoma13.jpg Courtesy of: <https://thepeninsulaqatar.com/article/21/10/2015/Over-11-moles-on-arm-can-predict-deadly-skin-cancer-risk>

Melanoma14.jpg Courtesy of: ISIC

Melanoma15.jpg Courtesy of: ISIC

Melanoma16.jpg Courtesy of: <https://www.harrisdermatology.com/news/skin-cancer-in-skin-of-color-signs-you-may-miss/>

Melanoma17.jpg Courtesy of: <https://www.healthline.com/health/melanoma-pictures>

Melanoma18.jpg Courtesy of: <https://emedicine.medscape.com/article/1100753-overview>

Melanoma19.jpg Courtesy of: <https://www.medicalnewstoday.com/articles/melanoma-on-black-skin>

Melanoma20.jpg Courtesy of: <https://www.mymelanomateam.com/resources/types-of-melanoma-skin-cancer-photos-and-symptoms>

Melanoma(21-33).jpg Courtesy of: ISIC

Melanoma(34-35).jpg Courtesy of: <https://pmc.ncbi.nlm.nih.gov/articles/PMC4113154/>

Melanoma36.jpg Courtesy of: <https://www.asds.net/skin-experts/skin-cancer/skin-cancer-in-people-of-color/skin-cancer-photo-gallery>

Melanoma37.jpg Courtesy of: <https://www.skintherapyletter.com/skin-cancer/melanoma/>

Melanoma38.jpg Courtesy of: <https://www.skin55.co.uk/malignant-melanoma>

Melanoma39.jpg Courtesy of: <https://abcnews.go.com/Health/cancerous-melanomas-skin-deep/story?id=54987809>

Melanoma40.jpg Courtesy of: ISIC

Mole1.jpg Courtesy of: <https://www.skinvision.com/moles-pictures/>

Mole2.jpg Courtesy of: <https://southeastskinclinic.com.au/skinclinic/mole/>

Mole3.jpg Courtesy of: <https://www.aimatmelanoma.org/melanoma-101/understanding-melanoma/moles-and-other-lesions/types-moles-skin-lesions/>

Mole4.jpg Courtesy of: CDSS

Mole5.jpg Courtesy of: CDSS

Mole6.jpg Courtesy of: <https://www.aocd.org/page/Moles>

Mole(7-23).jpg Courtesy of: ISIC

OtherLesion(1-8).jpg Courtesy of: ISIC